Geophysical Research Letters

RESEARCH LETTER
10.1029/2024GL114394

The Effect of Water Vapor and Solar Zenith Angle on Oceanic Diurnal Warming

Andrew Harris[1], **Gary Wick**[2], **and Sandra Castro**[3]

[1]Earth System Science Interdisciplinary Center, NOAA Cooperative Institute for Satellite Earth System Studies, University of Maryland, College Park, MD, USA, [2]Physical Sciences Laboratory, NOAA, Boulder, CO, USA, [3]Colorado Center for Astrodynamics Research, University of Colorado Boulder, Boulder, CO, USA

Key Points:

- Reliable modeling of oceanic diurnal warming is both desirable and challenging to achieve consistently on the global scale
- Accounting for atmospheric and in-water effects due to varying water vapor and solar zenith angle produces substantial changes in warming
- The new insolation scheme shows improvement cf. a similarly derived set of static coefficients when compared to satellite observations

Supporting Information:

Supporting Information may be found in the online version of this article.

Correspondence to:

A. Harris,
aharris2@umd.edu

Citation:

Harris, A., Wick, G., & Castro, S. (2025). The effect of water vapor and solar zenith angle on oceanic diurnal warming. *Geophysical Research Letters*, *52*, e2024GL114394. https://doi.org/10.1029/2024GL114394

Received 23 DEC 2024
Accepted 15 APR 2025

Author Contributions:

Conceptualization: Andrew Harris
Data curation: Gary Wick, Sandra Castro
Formal analysis: Andrew Harris
Investigation: Gary Wick
Methodology: Andrew Harris, Gary Wick
Resources: Gary Wick
Software: Andrew Harris, Gary Wick
Supervision: Andrew Harris
Validation: Gary Wick, Sandra Castro
Visualization: Andrew Harris, Gary Wick
Writing – original draft: Andrew Harris
Writing – review & editing: Andrew Harris, Gary Wick, Sandra Castro

Abstract Oceanic diurnal warm layers have been extensively studied over the years due to their important role in a variety of geophysical disciplines. Much of this research has been dedicated to the development of predictive models of varying complexity to calculate the spatiotemporal magnitude of the effect. This manuscript presents results which show that significant variability can be accounted for by addressing the combined impacts of atmospheric water vapor and solar zenith angle on both the spectral distribution of insolation energy at the water surface and its subsequent absorption within the water column. Comparisons with satellite-observed diurnal amplitudes on the basin-scale show that the new scheme provides notable improvements over one with a fixed insolation parameterization. One implication is that addressing the heat source term within the water column is a key first step when developing and tuning models of the diurnal layer.

Plain Language Summary Reliable modeling of the oceanic diurnal warm layer is needed for improved understanding of several geophysical processes, and for analysis of satellite data. To date, obtaining consistent estimates of warming on a global basis has proved challenging. We show that careful accounting for spectral variations in incoming solar energy due to angle and water vapor produces significantly different patterns of warming when compared to a more typical static approach. Comparisons of modeled versus satellite-observed oceanic warming show that the new scheme provides more consistent warming estimates on the basin-scale.

1. Introduction

The ability to model the physical processes of upper-ocean warming accurately is key to understanding a number of important processes in the climate system. The skin layer itself is the interface between ocean and atmosphere, both governing and responding to ocean-atmosphere fluxes of heat and gas exchange (e.g., Fairall et al., 1996; Robertson & Watson, 1992; Siegenthaler & Sarmiento, 1993; Watson et al., 2020; Zhang et al., 2021). The distribution of heat in the near-surface is a precursor to vertical transport for seasonal development of the mixed layer as well as entrainment of heat to the ocean interior. Modeling these processes correctly is important—recent data sets of sub-thermocline ocean heat content have shown that is where excess heat due to Earth Energy Imbalance is going (e.g., Cheng et al., 2017; Levitus et al., 2012) but this was not well-predicted by many coupled climate models (e.g., Cheng et al., 2016). The process is also important for understanding and using observations of sea surface temperature (SST), especially from satellite. Satellite observations of SST outnumber other sources by several orders of magnitude, so the question arises as to how best to treat them. Since all satellite-based measurements are either sensitive to the temperature in the top few microns (thermal infrared) or millimeters (microwave), accounting for any differences between this and the temperature at depth is key to ensure correct assessment of the thermodynamic heat content of the ocean (e.g., Rayner et al., 2006). Finally, knowledge of the oceanic skin temperature is important for assimilation of satellite radiances into atmospheric models (e.g., Akella et al., 2017; Massart et al., 2021). The latter requirement stems from the need for an accurate skin temperature to obtain good results for lower atmospheric sounding due to the surface contribution in channel weighting functions that intersect the surface.

In recent years, the importance of diurnal warm layer, especially when considering satellite SSTs, has come to the fore (e.g., Cronin et al., 2024). A number of studies have observed diurnal excursions of skin SST in excess of 5 K (e.g., Flament et al., 1994; Gentemann et al., 2008). While such warming magnitudes cannot be produced in standard ocean models, primarily due to the vertical resolution and concomitant heat capacity of the topmost

layer, there is renewed interest in predicting such excursions, either by parameterization (e.g., Zeng & Beljaars, 2005) or more detailed modeling (e.g., Karagali et al., 2017).

The primary heat source for the ocean is incoming solar radiation. The longwave part of the solar spectrum is strongly absorbed in the near-surface (~25% in the top few cm). Because the absorption of red, and especially near-IR wavelengths, is so strong, in-water absorption of solar radiation is often parameterized as only a few exponential absorbing functions (sometimes as few as 2, e.g., Paulson & Simpson, 1977), with the shorter wavelengths being absorbed much more slowly (1/*e* depths of order meters rather than cm-to-mm). Much effort has been expended in accounting for variations in the absorption profile of the more penetrating radiation, primarily in terms of ocean biology, evolving from Jerlov water type to chlorophyll concentration, $K_{d(490)}$, suspended sediment, and so forth (e.g., see Morel & Antoine, 1994; Ohlmann & Siegel, 2000). The longer wavelengths are essentially unaffected by such processes, are absorbed almost completely within the top layer of a typical ocean model, and have received comparatively little attention.

2. Materials and Methods

We have implemented a refined treatment for the absorption of solar radiation within a diurnal warming model that is run in a 1-D sense at individual points on a global grid (to 60°N/S). The model is based originally on the Kantha and Clayson (1994, hereafter KC94) turbulence closure scheme with the Kantha and Clayson (2004) modification that includes a parameterization for Stokes' drift. Further refinements include exponentially increasing model layer thickness from 0.005 m within the top 0.025–1 m between 16 and 50 m depth. This model may be considered to be representative of the more sophisticated diffusion schemes, and therefore serves as a useful test-bed for assessing both the current state of knowledge and evaluating further improvements.

Our refined approach focuses on atmospheric impacts on the in-water absorption of solar radiation at the long, near-IR wavelengths. Since there is no partitioning of solar radiation flux in Numerical Weather Prediction (NWP) output, the fractional distribution of incoming radiation with wavelength is essentially fixed. Although the fraction of radiation in the near-IR is relatively small, the corresponding very short 1/*e* depths mean that the heating rate, and therefore buoyancy production, is intense. However, under high water vapor loadings in the tropics (~60 $kg.m^{-2}$), the fraction of radiation in the near-IR reaching the ocean surface is substantially reduced, leading to less intense stratification and concomitantly greater heat penetration under mixing.

To assess the magnitude of these atmospheric effects, we have developed an initial scheme for insolation parameterization as a function of total column water vapor. Because the path of dry air absorption also changes for each band with solar zenith angle, the parameterization takes the form of a multidimensional lookup table to ensure that the effects can be separated. The previous insolation parameterization is the widely used (e.g., KC94; Paulson & Simpson, 1981; Sweeney et al., 2005) scheme that partitions information on fractional radiation and 1/*e* depth into 9 wavebands (sourced from Defant, 1961, following Schmidt, 1908) to obtain a composite function of the heating rate profile. While the waveband definitions were retained given the wide use of the 9-band Defant model, the 1/*e* depths for in-water absorption were revisited since the original values are over a century old.

Solar radiative transfer calculations were performed at 1 cm^{-1} resolution using MODTRAN4 and a globally representative set of atmospheric profiles over the ocean sampled from ECMWF data, with solar radiation fractions being calculated for the same wavebands as those of Defant. Solar zenith angles were selected corresponding to airmass values of 1, 1.5, 2, 3, 5, and 10 (approximately 0, 48, 60, 70, 78, and 84 degrees), with total column water vapor amounts binned in 5 $kg.m^{-2}$ intervals, resulting in 13 bin means ranging from 3.8 to 61.8 $kg.m^{-2}$. For the full 2-dimensional case, in-water refraction is accounted for using a First order approximation of a plane surface, and refractive index 1.33 for all wavelengths, giving a path length scaling of $\{\cos[\sin^{-1}(\sin(\text{solar-zenith-angle})/1.33)]\}^{-1}$. To account for correlation between atmospheric and in-water absorption features, Segelstein (1981, hereafter S81) complex refractive index data were convolved with the 1-wavenumber MODTRAN output and radiance-weighted 1/*e* depths calculated for every simulated atmospheric spectrum prior to averaging across each waveband. Although the S81 data are for pure water, the effect of salinity is minor outside of microwave frequencies, and negligible for visible wavelengths that have significant penetration (Mobley, 1994). The corresponding composite normalized irradiance profiles can be seen in Figure 1, which also shows the profile for a static set of coefficients taken from the MODTRAN4 output for the 48° case, integrated over the range of water vapor loadings, as well as the original Defant 9-band absorption scheme. These static coefficients are intended to approximate the "average" effect of the new scheme and facilitate later comparison of the explicit

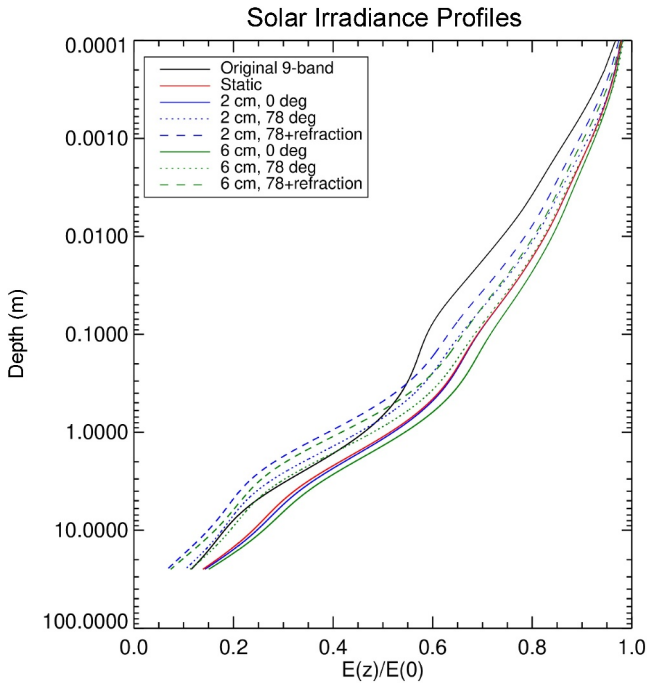

Figure 1. Normalized solar irradiance with depth. Solid black line is original 9-band Defant. Red line is static equivalent. Other lines illustrate different water vapor amounts and solar zenith angles.

2-D dependence. The figure also illustrates the importance of including refraction for larger solar zenith angles. Although the insolation values will be lower in such circumstances, this factor becomes increasingly important at higher latitudes, where lower sun angles predominate (N.B. solar zenith angles of zero do not exist outside of the tropics—this also guided the selection of the 48° subset to serve as the static case). Although the new absorption scheme generally shows less strong absorption than the original Defant near the surface due to atmospheric absorption, the absorption curves for the 78° case do cross over the latter at a depth of 0.3–0.4 m reflecting the deeper penetration.

The temporal evolution of the temperature profile for an idealized forcing run with a constant U_{10} = 1 m.s^{-1} wind speed and peak insolation of 1,000 W.m^{-2} is shown in Figure 2. The left-hand panel depicts the results for the standard Defant 9-band insolation scheme, using turbulence parameters that have yielded realistic diurnal SST amplitudes relative to past cruise observations (Wick et al., 2022). The center panel shows the similar warming profiles for the same model configuration but utilizing the static coefficients (48°) for the new absorption scheme. The decrease in near-surface absorption (as illustrated in Figure 1) results in substantial reduction of the near-surface peak warming. Since the previous model configuration with the original absorption scheme produced realistic diurnal warming amplitudes, the turbulence parameters were adjusted to produce a maximum temperature excursion comparable to that of the original configuration. The right-hand panel shows the resultant temperature profile evolution with both the new absorption scheme and modified turbulence parameters. This new model configuration allows comparison of the diurnal amplitudes obtained using the full 2-D (varying water vapor and solar zenith angle) insolation scheme against those obtained using the same turbulence parameters but with static band-weight and 1/*e* depth coefficients.

Simulations of the daily diurnal warming amplitude were generated using the modified 1-D KC model over the ±60° latitude grid using the new insolation scheme with both the full 2-D and simplified static coefficients for the months of July 2019 and March 2020. Similar to Wick et al. (2024), the forcing data is sourced from NCEP GFS

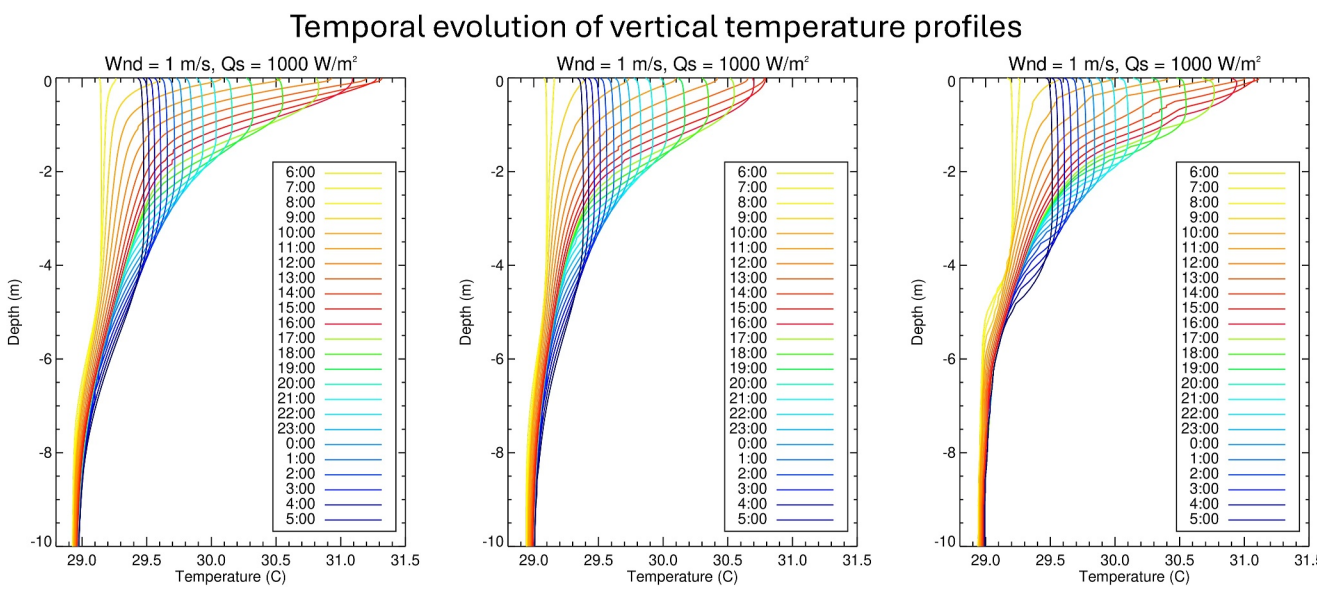

Figure 2. Temporal evolution of near surface temperature profile. Incoming solar radiation calculated for tropics (1,000 W.m^{-2} peak, 12 hr sunlight). Left panel: original Defant 9-band in-water absorption. Center panel: new absorption, original turbulence parameters; Right-panel: new absorption, modified turbulence parameters.

0.5° fields, including net shortwave (which utilizes an angle-dependent ocean albedo, Briegleb et al., 1986) and longwave radiation fluxes, latent and sensible heat, ocean temperature (required for the equation of state), wind stress, and parameters from the Wavewatch III model (significant wave height, primary wave period, primary wave direction). The model is run individually for each grid cell using a 5-min timestep, with insolation values interpolated using cloud fraction estimates and an idealized curve for solar radiation, normalized by the NCEP shortwave flux. Other flux values are obtained by linear interpolation to each timestep. The model is run for a full 48 hr, with warming values taken for the second 24-hr period (the day in question), and then reinitialized to a uniform temperature with depth before the next run. The daily diurnal warming amplitude at each cell is derived from hourly output temperatures at the top layer of the model. The constraint to ±60° latitude circumvents potential issues with sea ice and continuous solar radiation during summer months at high latitudes, while still allowing comparisons against geostationary satellite observations.

3. Results and Discussion

Figures 3a and 3b show comparisons of the 90th and 50th percentile of peak daily warming values for the full 2-D and static insolation schemes calculated for July 2019. While values of up to ∼4 K are modeled in both cases (not shown, but see Wick et al., 2024), the difference plots reveals a distinct pattern of water vapor suppressing the diurnal amplitudes at low latitudes, with the depression in the vicinity of the Warm Pool being particularly evident. Additionally, a combination of higher solar zenith angles and lower water vapor appears to have enhanced the warming at higher latitudes.

Figures 3c and 3d shows the same comparisons, but for March 2020, that is, around the equinox, where the Sun is more directly overhead in the tropics. This time, the suppression due to water vapor is more pronounced, stretching across the entire tropics, while the enhancement at higher solar zenith angles (and lower water vapor) is still evident. With respect to the issues raised previously regarding the challenge of obtaining diurnal amplitude estimates that perform reliably across the globe, this reduction in warmings for the tropics cf. those observed at higher latitudes for N Hemisphere summer should be considered a desirable trait. The potential to reduce the diurnal amplitude in the tropics relative to higher latitudes while preserving global average amplitude values is consistent with expectations for needed corrections associated with unaccounted-for changes in the spectral content of surface solar radiation and suggests that the new scheme has the potential to produce diurnal SST amplitudes that perform more reliably across the globe.

The zonal distribution of the fractional depression for all significant (>0.1 K) warmings relative to those modeled using static coefficients is shown in the bottom panel of Figure 3. The location of the peak depression in warming moves in a manner consistent with the location of the ITCZ, being further north in July than March. The enhancement of fractional warming is asymmetrical with respect to latitude in July, most likely due to the reduced range of solar zenith angles in the northern hemisphere cf. the southern hemisphere. This information is not obvious from the upper panel of Figure 3 since the absolute warming values are significantly larger in the northern hemisphere. As might be expected, the fractional warming behavior is more symmetrical for March 2020. At this point, it is worth reiterating that the curves shown for July 2019 and March 2020, and the spatial patterns shown in Figure 3, are solely due to the adoption of a 2-dimensional water vapor and solar zenith angle dependent shortwave absorption scheme versus a static set of coefficients. There are no other differences in model physics.

The above results illustrate the importance of ensuring that the heat source term within the water column is correctly accounted for at every time step. The question arises as to the usefulness of the new model configuration beyond this perturbation experiment and consistency with available observations of diurnal SST amplitude. To assess this, SST retrievals from the Advanced Himawari Imager (AHI) carried on Himawari-8 (H8) and the Advanced Baseline Imager (ABI) carried on GOES-16 (G16) are used to obtain daily diurnal warming amplitudes following Wick and Castro (2020). The SST products used for this are NOAA's Advanced Clear Sky Processor for Oceans Level-2C (ACSPO L2P) data. The ACSPO SST retrievals from the ABI and AHI have high sensitivity to SST (Petrenko et al., 2019), primarily due to more channels and lower noise than previous-generation geostationary imagers, which is an important characteristic for this analysis. Amplitudes of satellite-observed diurnal warming are matched with the daily estimates from the model configuration with new 2-D absorption coefficients and modified turbulence parameters for July 2019 and March 2020. The advantage of such an approach is that results are obtained on the basin-scale, rather than for geographically limited cruise data, even though the latter are of higher accuracy.

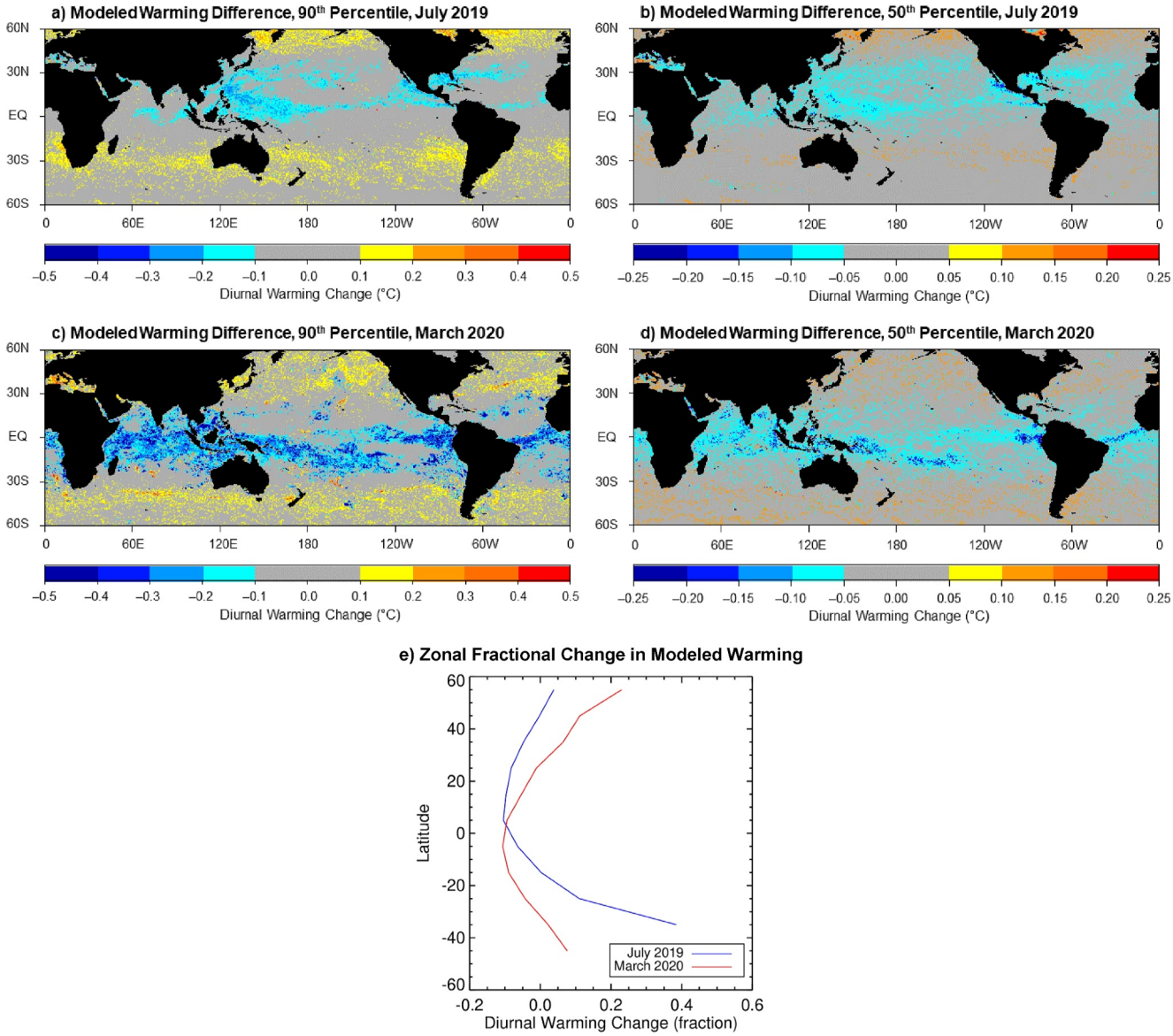

Figure 3. Top panels shows difference in 90th (a) and 50th (b) percentile peak warming values between modeling using full 2-D absorption scheme and static 48° coefficients, for July 2019. Middle panels (c, d) are for March 2020. Bottom plot (e) shows corresponding zonal mean fractional change for all calculated warmings.

Additionally, the use of NWP forcing fluxes should provide validation more indicative of real-world operational performance. Figure 4 shows the results of point-for-point diurnal matches for both H8 and G16. The main result to note is that, while there is significant scatter in the results, the observed and modeled warmings are distributed about the 1:1 line. The scatter is primarily due to a combination of the highly nonlinear nature of diurnal warming at low wind speeds and the accuracy of the forcing fluxes. (N.B. Wind mixing energy is proportional to ρu^{*3}, thus there is nearly an order of magnitude more for a wind speed of 2 m.s^{-1} than 1 m.s^{-1}.) Still, the results suggest that the new absorption scheme can potentially reproduce the global range of observed diurnal warming amplitudes.

One issue that can arise with such comparisons is the introduction of aliasing due to spatiotemporal mismatch, generally arising from slight timing errors in the NWP field. An alternative way of analyzing the data is to construct PDFs of observed and modeled warming. Figure 5 shows the PDFs of observed and modeled warming for H8 and G16. The plots also show the results obtained from the model utilizing only the static solar absorption coefficients. In almost every case, the 2-D absorption scheme outperforms the static configuration, particularly at low-to-moderate warmings. The main exception appears to be for warmings above ~2.5 K for the H8 data in

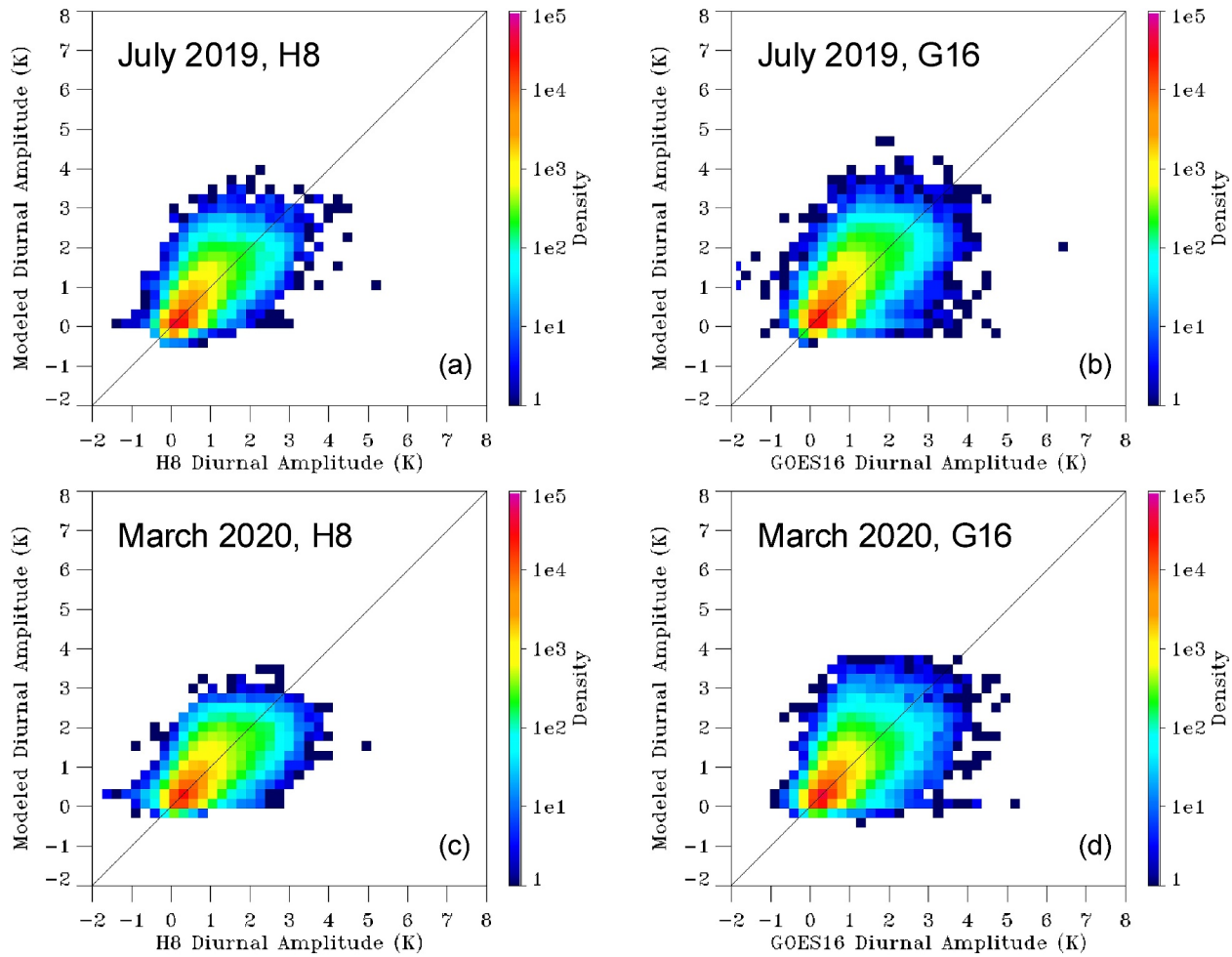

Figure 4. Comparison of new DW predictions with full 2-D code and in-water refraction compared with H-8 (left column) and G-16 (right column) observations. Top row is for July 2019; bottom row is for March 2020.

March 2020. Both schemes seem to underestimate warming cf. observations, and the reduction in large warmings due to the suppression of near-IR shortwave by water vapor increases the discrepancy.

4. Conclusion

We have shown the importance of accounting for atmospheric and in-water effects due to water vapor and solar zenith angle when modeling the global distribution of diurnal SST amplitude. These factors, which are typically neglected, directly affect the heat source term within the water column. Parallel work has more extensively demonstrated the accuracy of the underlying diurnal warming model with the original solar absorption scheme and its sensitivity to different turbulence configurations (Wick et al., 2022, 2024). The results here show comparable spread in the predicted-observed differences and show that the semi-empirical turbulence constants in the model can be tuned to different insolation schemes. Capturing the initial distribution of heat is fundamental and should be a critical part of deriving a final recommended model configuration. The parameters required for this scheme are readily available along with the necessary NWP forcing data.

Next steps to improve upon this initial analysis are readily apparent. The methodology currently relies on the albedo adjustment inherent in the NWP net shortwave flux calculations, which lacks spectral discrimination. Additional radiative transfer calculations we have performed show that spectral adjustment due to cloud amount (and type, especially water vs. ice) is warranted, although most large warmings occur in the absence of significant cloud. Global data sets now exist to facilitate further integration of the ocean biology component into the in-water absorption (e.g., Liu & Wang, 2022). Additionally, the in-water normalized solar irradiance at high (1 cm^{-1})

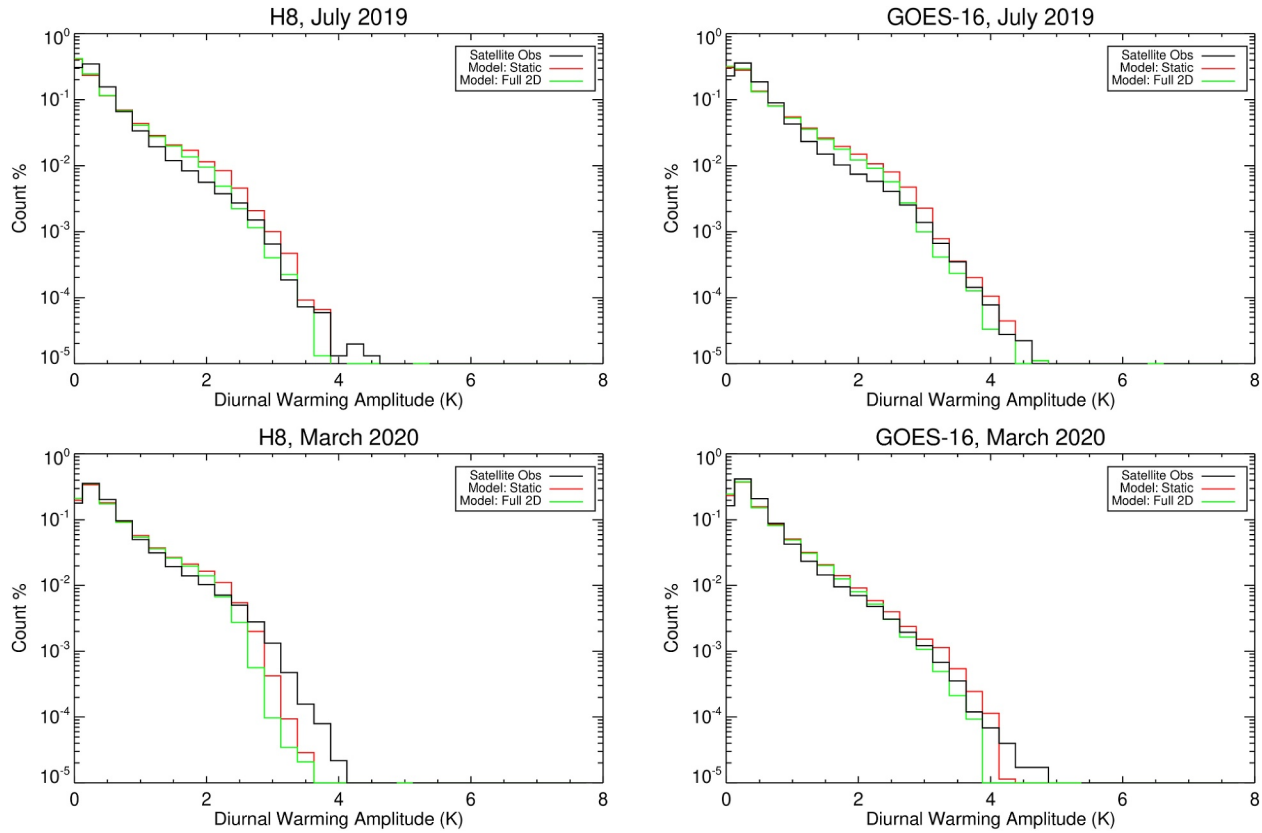

Figure 5. Probability density functions for modeled and observed warming, with panel layout as in Figure 4. Satellite observations are plotted in black. The full 2-D modeling is shown in green, while the static coefficients are plotted in red.

resolution has a smoother profile than the 9-band scheme (see Text S1 in Supporting Information S1) so the band selection could benefit from being optimized. All of these will impact the heat source term within the water column. While the relative performance of different NWP data sets could introduce regional discrepancies, initial testing suggests this is not a major effect. Reducing errors due to the above-mentioned factors is highly desirable before attempting final tuning of intrinsic model turbulence parameters.

Data Availability Statement

The primary solar zenith angle and total column water vapor dependent lookup tables for Planck weighting and in-water 1/*e* depths for the 9-band model are available at https://doi.org/10.5061/dryad.4qrfj6qhj along with the MODTRAN4 output, total column water vapor values, and S81 absorption data for pure water. Diurnal model outputs and satellite validation data are cited in companion paper (Wick et al., 2024).

Acknowledgments
This study was supported by NOAA Grant NA19NES4320002 (Cooperative Institute for Satellite Earth System Studies - CISESS) at the University of Maryland/ESSIC.

References

Akella, S., Todling, R., & Suarez, M. (2017). Assimilation for skin SST in the NASA GEOS atmospheric data assimilation system. *Quarterly Journal of the Royal Meteorological Society*, *143*(703), 1032–1046. https://doi.org/10.1002/qj.2988

Briegleb, B. P., Minnis, P., Ramanathan, V., & Harrison, E. (1986). Comparison of regional clear-sky albedos inferred from satellite observations and model computations. *Journal of Applied Meteorology and Climatology*, *25*(2), 214–226. https://doi.org/10.1175/1520-0450(1986)025<0214:corcsa>2.0.co;2

Cheng, L., Trenberth, K. E., Fasullo, J., Boyer, T., Abraham, J., & Zhu, J. (2017). Improved estimates of ocean heat content from 1960 to 2015. *Science Advances*, *3*, e1601545. https://doi.org/10.1126/sciadv.1601545

Cheng, L., Trenberth, K. E., Palmer, M. D., & Abraham, J. P. (2016). Observed and simulated full-depth ocean heat-content changes for 1970-2005. *Ocean Science*, *12*(4), 925–935. https://doi.org/10.5194/os-12-925-2016

Cronin, M. F., Zhang, D., Wills, S. M., Reeves Eyre, J. E. J., Thompson, L., & Anderson, N. (2024). Diurnal warming rectification in the tropical Pacific linked to sea surface temperature front. *Nature Geoscience*, *17*(4), 316–322. https://doi.org/10.1038/s41561-024-01391-8

Defant, A. (1961). *Physical oceanography* (Vol. I, p. 729). Pergamon Press.

Fairall, C. W., Bradley, E. F., Godfrey, J. S., Wick, G. A., Edson, J. B., & Young, G. S. (1996). Cool-skin and warm layer effects on sea surface temperature. *Journal of Geophysical Research*, *101*(C1), 1295–1308. https://doi.org/10.1029/95jc03190

Flament, P., Firing, J., Sawyer, M., & Trefois, C. (1994). Amplitude and horizontal structure of a large sea surface warming event during the Coastal Ocean Dynamics Experiment. *Journal of Physical Oceanography*, *24*, 124–139.

Gentemann, C. L., Minnett, P. J., LeBorgne, P., & Merchant, C. J. (2008). Multi-satellite measurement of large diurnal SST warming events. *Geophysical Research Letters*, *35*(22), L22602. https://doi.org/10.1029/2008gl035730

Kantha, L. H., & Clayson, C. A. (1994). An improved mixed layer model for geophysical applications. *Journal of Geophysical Research*, *99*(C12), 25235–25266. https://doi.org/10.1029/94jc02257

Kantha, L. H., & Clayson, C. A. (2004). On the effect of surface gravity waves on mixing in the oceanic mixed layer. *Ocean Modelling*, *6*(2), 101–124. https://doi.org/10.1016/s1463-5003(02)00062-8

Karagali, I., Hoyer, J. L., & Donlon, C. J. (2017). Using a 1-D model to reproduce the diurnal variability of SST. *Journal of Geophysical Research: Oceans*, *122*(4), 2945–2959. https://doi.org/10.1002/2016JC012542

Levitus, S., Antonov, J. I., Boyer, T. P., Baranova, O. K., Garcia, H. E., Locarnini, R. A., et al. (2012). World ocean heat content and thermosteric sea level change (0–2000 m), 1955–2010. *Geophysical Research Letters*, *39*(10), L10603. https://doi.org/10.1029/2012gl051106

Liu, X., & Wang, M. (2022). Global daily gap-free ocean color products from multi-satellite measurements. *International Journal of Applied Earth Observation and Geoinformation*, *108*, 102714. https://doi.org/10.1016/j.jag.2022.102714

Massart, S., Bormann, N., Bonavita, M., & Lupu, C. (2021). Multi-sensor analyses of the skin temperature for the assimilation of satellite radiances in the European centre for medium-range weather forecasts (ECMWF) integrated forecasting system (IFS, cycle 47R1). *Geoscientific Model Development*, *14*(9), 5467–5485. https://doi.org/10.5194/gmd-14-5467-2021

Mobley, C. D. (1994). Optical properties of water. In M. Bass (Ed.), *Handbook of optics* (Vol. 1). McGraw-Hill.

Morel, A., & Antoine, D. (1994). Heating rate within the upper ocean in relation to its bio-optical state. *Journal of Physical Oceanography*, *24*(7), 1652–1665. https://doi.org/10.1175/1520-0485(1994)024<1652:hrwtuo>2.0.co;2

Ohlmann, J. C., & Siegel, D. A. (2000). Ocean radiant heating. Part II: Parameterizing solar radiation transmission through the upper ocean. *Journal of Physical Oceanography*, *30*(8), 1849–1865. https://doi.org/10.1175/1520-0485(2000)030<1849:orhpip>2.0.co;2

Paulson, C. A., & Simpson, J. J. (1977). Irradiance measurements in the upper ocean. *Journal of Physical Oceanography*, *7*(6), 952–956. https://doi.org/10.1175/1520-0485(1977)007<0952:imituo>2.0.co;2

Paulson, C. A., & Simpson, J. J. (1981). The temperature difference across the cool skin of the ocean. *Journal of Geophysical Research*, *86*(11), 11044–11054. https://doi.org/10.1029/jc086ic11p11044

Petrenko, B., Ignatov, A., Kihai, Y., & Pennybacker, M. (2019). Optimization of sensitivity of GOES-16 ABI sea surface temperature by matching satellite observations with L4 analysis. *Remote Sensing*, *11*(2), 206. https://doi.org/10.3390/rs11020206

Rayner, N. A., Brohan, P., Parker, D. E., Folland, C. K., Kennedy, J. J., Vanicek, M., et al. (2006). Improved analyses of changes and uncertainties in sea surface temperature measured in situ since the mid-nineteenth century: The HadSST2 dataset. *Journal of Climate*, *19*(3), 446–469. https://doi.org/10.1175/jcli3637.1

Robertson, J. E., & Watson, A. J. (1992). Thermal skin effect of the surface ocean and its implications for CO_2 uptake. *Nature*, *358*(6389), 738–740. https://doi.org/10.1038/358738a0

Schmidt, W. (1908). Absorption der sonnenstrahlung im wasser. *SB Akad. Wiss. Wien*, *117*, 237–253.

Segelstein, D. J. (1981). *The complex refractive index of water*. MSc Thesis (p. 175). University of Missouri-Kansas City.

Siegenthaler, U., & Sarmiento, J. L. (1993). Atmospheric carbon dioxide and the ocean. *Nature*, *365*(6442), 119–125. https://doi.org/10.1038/365119a0

Sweeney, C., Gnanadesikan, A., Griffies, S. M., Harrison, M. J., Rosati, A. J., & Samuels, B. L. (2005). Impacts of shortwave penetration depth on large-scale ocean circulation and heat transport. *Journal of Physical Oceanography*, *35*(6), 1103–1119. https://doi.org/10.1175/jpo2740.1

Watson, A. J., Schuster, U., Shutler, J. D., Holding, T., Ashton, I. G. C., Landschützer, P., et al. (2020). Revised estimates of ocean-atmosphere CO_2 flux are consistent with ocean carbon inventory. *Nature Communications*, *11*(1), 4422. https://doi.org/10.1038/s41467-020-18203-3

Wick, G. A., & Castro, S. L. (2020). Assessment of extreme diurnal warming in operational geosynchronous satellite sea surface temperature products. *Remote Sensing*, *12*(22), 3771. https://doi.org/10.3390/rs12223771

Wick, G. A., Castro, S. L., Harris, A., & Mittaz, J. (2024). Evaluation of modeled diurnal warming estimates for application to producing SST analyses. *Earth and Space Science*, *11*(9), e2024EA003619. https://doi.org/10.1029/2024EA003619

Wick, G. A., Castro, S. L., Harris, A., Mittaz, J., & Maturi, E. (2022). Evaluation of modeled diurnal warming estimates for application to producing SST analyses, OS15B-0778. In *2022 fall AGU meeting, Chicago, IL*.

Zeng, X., & Beljaars, A. (2005). A prognostic scheme of sea surface skin temperature for modeling and data assimilation. *Geophysical Research Letters*, *32*(14), L14605. https://doi.org/10.1029/2005gl023030

Zhang, R., Zhou, F., Wang, X., Wang, D., & Gulev, S. K. (2021). Cool skin effect and its impact on the computation of the latent heat flux in the South China Sea. *Journal of Geophysical Research: Oceans*, *126*(1), e2020JC016498. https://doi.org/10.1029/2020jc016498